JOURNAL OF PROPULSION AND POWER
Vol. 20, No. 3, May–June 2004

Two-Phase Modeling of Hydrodynamic Instabilities in Coaxial Injectors

Byoung-Do Kim[*] and Stephen D. Heister[†]
Purdue University, West Lafayette, Indiana 47907

The hydrodynamic instability of coaxial injectors with recessed inner fluid posts have been investigated using a homogeneous flow method with in a time-dependent, viscous calculation. The focus is on the unsteady self-oscillation mode observed in the submerged portion of the injector. Because of the large difference between gas and liquid velocities, the Kelvin–Helmholtz instability mechanism plays a prominent role in the unsteady behavior. A two-dimensional analog is investigated to assess the influence of various flow and geometric parameters on the instability. Both amplitude and frequency of oscillations are characterized for gas/liquid streams of various velocities, densities, and viscosities. The effect of the length of the submerged passage and the thickness of the inner post are also studied in detail. Unsteady, quasi-periodic oscillations are observed in nearly all cases.

Nomenclature

f = frequency
h = liquid sheet half thickness (Figs. 1 and 5)
k = wave number
L = length of submerged channel (Fig. 5)
$\dot{m}$ = mass flow
n = number of sheet thicknesses in channel height (Fig. 4)
P = pressure
R = radius of curvature
Re = Reynolds number
t = time
t_{LOX} = liquid oxygen post thickness (Fig. 5)
U = reference (dimensional) axial velocity
u = axial velocity
V_c = cell volume
v = transverse velocity
x = axial coordinate
y = transverse coordinate
α = void fraction
ϵ = gas/liquid density ratio
η = perturbation in sheet height
μ = viscosity
ρ = fluid pseudodensity
σ = surface tension
ω = disturbance frequency

Subscripts

g = gas
l = liquid

Introduction

IN many coaxial injectors, liquid flowing down a central post is atomized by a high-velocity gas passing around the outer annulus. In many applications, the liquid post is submerged somewhat from the orifice exit plane to provide flame holding in combustion systems such as liquid rocket engines. High-frequency oscillation of the jet spray has been observed in experimental studies of coaxial injectors with a submerged liquid post.[1–7] These disturbances could couple with the dynamics of the jet breakup process and potentially provide amplification of oscillations within the combustion chamber. Bazarov and Yang[2] and Bazarov and Lyul'ka[2] called this phenomenon self-oscillation and suggested this as a cause of decreased combustion efficiency and a source of high-amplitude noise during combustion. Combustion instabilities of this nature can have severe impact on the performance of the engine and can in some cases lead to catastrophic failures.

Hutt and Rocker[8] investigated the high-frequency combustion instability associated with coaxial injectors. They classified the instability phenomena in the chamber as injection coupled and intrinsic mechanisms. The injection coupling implies chamber pressure/temperature variation as a key contributor in the change of flow dynamics through the injector. In the other hand, the intrinsic mechanism occurs in the flowfield due to its own flow dynamics with negligible feed system effect. However, note that injection coupling is never independent of the intrinsic subprocesses, such as atomization, propellant heatup, vaporization, and mixing because these processes determine the relationship between the injector response and the chamber response.

Bazarov and Yang[1] and Bazarov and Lyul'ka studied the self-oscillation phenomena along with the self-pulsation mode of jet instability in coaxial injector. They postulated that self-oscillation occurs when the gas/liquid interaction forms a cavity inside nozzle, leading to jet swirling around the nozzle exit. The self-pulsation of the liquid jet mixed with the gas flow depends on the pressure drop at liquid and gas phases, correlating with the time of liquid propagation through the injector nozzle.[9] In addition to external disturbances from combustion chamber and feed system during engine operation, injectors can generate self-pulsation under certain conditions by its own intrinsic unsteadiness, leading to random modeification of the spray formation process.

Mayer and his research group have studied the coaxial injector in terms of the combustion instability. Mayer and Krulle[4] investigated coaxial flow mixing phenomena in terms of chamber pressure variation, density/velocity ratio changes, and surface tension effect. When chamber pressure is increased, gas density is increased, magnifying the aerodynamic interaction between the liquid and gas phases and resulting in a faster, finer atomization. Increasing surrounding gas velocity also leads to an increase of surface wave growth and to macroscopic instabilities of the liquid jet. They claimed the initiation of the jet surface deformation was due to internal liquid turbulence delivering energy in forms of eddy structures, approximately a size of 10–30% of the liquid oxygen (LOX) post diameter. In Refs. 5 and 6, the coaxial injector flow was studied under firing engine conditions at supercritical chamber pressure (higher than 5 MPa). The study revealed a remarkable difference

---

Received 18 February 2002; revision received 3 February 2003; accepted for publication 22 March 2003.

[*] Graduate Research Assistant, School of Aeronautics and Astronautics.
[†] Professor, School of Aeronautics and Astronautics.

between subcritical spray formation and the supercritical injection and mixing. At the subcritical condition, the liquid jet shows similar flow pattern to the cold-flow test, forming ligaments off the liquid jet surface and producing droplets before evaporation. On approaching and exceeding supercritical pressure, droplets no longer exist, and the liquid jet rapidly dissolves. The flame from the combustion chamber was anchored at the tip of the LOX post by flow recirculation eddies serving as a flame holder for steady-state combustion. The asymmetric flow oscillation was also reported in all experiments, but the source of the oscillation was not clearly stated.

Instability mechanisms in coaxial injectors were also investigated experimentally under noncombusting conditions by Glogowski et al.[10] and Glogowski and Micci.[11] Their experimental results showed that for the coaxial injector with a LOX post recessed into the fuel annulus, the injector transitioned into a condition of resonance characterized by a whistling noise. Significant modification to the overall structure of the spray due to the strong acoustic coupling between injector hydrodynamics and spray formation was also found. Without the recessed region, the injector operation produced a near resonance condition with a lower amplitude whistling noise but did not change the spray structure much. The recirculation by reverse flow near the recessed LOX post exit was also observed in this study. The effort to measure flow properties within the recessed region was not successful due to optical constraints and the small spatial and temporal scales involved.

Eroglu and Chigier[12] focused on the wave characteristics of a liquid jet from coaxial air-blast injector. They measured the frequency and wavelength of the jet issuing from the injector and found two dominant wave types: spanwise (dilational) and streamwise (sinuous) waves. The spanwise wave showed at a low relative jet velocity between the gas and liquid phases and the streamwise wave showed at a high relative jet velocity. Average wavelengths decreased with liquid and gas velocity. The frequency band of the jet oscillation increased with the liquid jet velocity.

Mansour and Chigier[13] conducted similar research on the liquid sheet instability issuing from the two-dimensional air-assisted nozzle. The results showed the same pattern as the Eroglu and Chigier study.[12] However, Mansour and Chigier's study probed higher velocity cases and confirmed that the frequency of the liquid sheet oscillation increased with coflowing gas velocity. This also indicates that the aerodynamic interaction between gas and liquid flows is the dominant factor for the flow oscillation.

In general, for the flow at high velocity, most researchers agree that the principal source introducing instability to the jet is from aerodynamic forces arising from the interaction of the liquid jet with the surrounding gas flow. Reynolds and Weber numbers are generally very high in these atomizers and aerodynamic forces are several orders of magnitude larger than capillary forces. The interaction between the liquid and gas phases mainly comes from different velocities of each phase. The velocity discontinuity in a homogeneous fluid results in wave growth on the interface, which is a common Kelvin–Helmholtz instability.

Most of the works summarized here mainly contributed to the investigation of flow phenomena outside of the injector after the injection. The inner flow structure in a recessed region of the coaxial injector has not been studied in detail because of difficulties in making experiemental observations in this region. However, because the upstream flow in a injector provides the initial condition for the entire spray evolution in the combustion chamber, work in this area is highly desirable. In this paper, the two-dimensional analog (a liquid sheet in a channel) of the coaxial injector will be studied numerically to characterize amplitude and frequency of oscillations of the inner liquid sheet. Whereas the actual instabilities are three-dimensional in nature, use of a two-dimensional analog permits a larger parametric study in the current computing environment. The model is described briefly in the following section; results of parametric studies are then summarized in the latter part of the paper along with the result of finite LOX post thickness modeling.

Linear Analysis

Liquid sheet instabilities have been analyzed by many researchers over the past several decades.[14–16]. However, the vast majority of these studies concerned unbounded sheets, and the effects of a bounded domain, that is, a sheet in a channel, have not been addressed in previous works. For this reason, results for this case are presented herein. Note that the approach based on linear stability theory can only evaluate the beginnings on the instability. As the amplitude of the disturbance grows, the linear assumptions soon become invalid. In addition, the presence of a finite length domain makes the connection to an infinite sheet stability analysis somewhat tenuous, that is, the injection exit plane is not treated in periodic boundary conditions typically used in linear studies. Even though the theoretical approach does not allow us to describe the jet instability in a complete structure, it provides a good starting point for predicting unstable, wave-type behavior of the jet with disturbances.

Consider a two-dimensional liquid sheet with density ρ_l, surface tension σ, and uniform thickness $2h$, moving at velocity U_l through an inviscid moving gas medium of density ρ_g at velocity U_g as shown in Fig. 1. The coordinates are chosen such that the direction of the x axis is parallel to the direction of the velocity U_l and U_g and the y axis is normal to the liquid sheet with its origin located at the midplane of the liquid sheet. Let the relative velocity ΔU represent the velocity difference between gas and liquid phases, $U_g - U_l$, that is, the reference frame is attached to the liquid phase. Finally, let nh represent the distance to the channel wall as measured from the channel centerline.

For antisymmetrical disturbances, the displacements of corresponding points on the two surfaces are equal in magnitude and in the same direction. Hence, the two interfaces are regarded to have the following form:

$$y = \pm h + \eta \tag{1}$$

$$\eta = \eta_0 e^{(\omega t + ikx)} \tag{2}$$

where $y = \pm h$ are the equilibrium positions of the two interfaces, that is, the position with no disturbances; η_0 is the initial amplitude of the wave and is taken to be much smaller than the half-width of the sheet, h; k is the wave number of the disturbance and $k = 2\pi/\lambda$, where λ is the wavelength of the disturbance; and $\omega = \omega_r + i\omega_i$ is a complex variable. The real part ω_r represents the rate of growth or decay of the disturbance, its imaginary part ω_i is 2π times the disturbance frequency, and $-\omega_i/k$ is the wave propagation speed of the disturbance.

Let $\phi = \phi_g + \Delta U x$ be the velocity potential of the gas phase, where the ϕ_g is the perturbation potential with ϕ_l as the perturbation velocity potential for the liquid phase. We will neglect viscosity for this analysis because the Reynolds numbers are quite high in practical devices. In this case, the Laplace equation, $\nabla^2\phi = 0$, governs this process. The linearized kinematic boundary condition for the liquid phase is

$$\frac{\partial \phi_l}{\partial y} = \frac{\partial \eta}{\partial t} \tag{3}$$

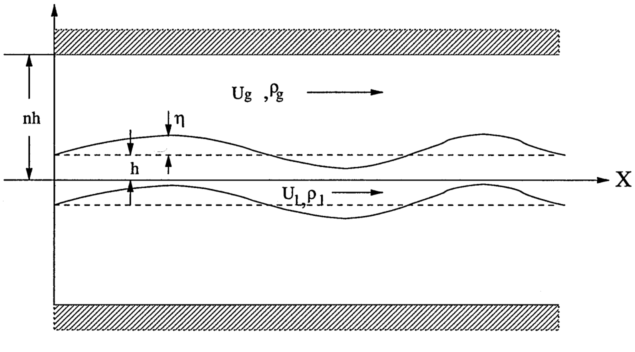

Fig. 1 Nomenclature for linear stability analysis for antisymmetric jet oscillations in a channel.

and for the gas phase

$$\frac{\partial \phi_g}{\partial y} = \frac{\partial \eta}{\partial t} + \Delta U \frac{\partial \eta}{\partial x} \tag{4}$$

which are to be satisfied at $y = \pm h$. The dynamic boundary condition from the unsteady Bernoulli's equation gives the following relation for the pressure at the interface:

$$P_l - P_g = -\rho_l \left(\frac{\partial \phi_l}{\partial t} \right) + \rho_g \left(\frac{\partial \phi_g}{\partial t} + \Delta U \frac{\partial \phi_g}{\partial x} \right) \tag{5}$$

The pressure jump induced by surface tension σ is

$$P_l - P_g = \frac{\sigma}{R} \cong -\sigma \frac{\partial^2 \eta}{\partial x^2} \tag{6}$$

to second order in η. Here, R is the radius of curvature of the interfaces. When the disturbances given in Eq. (2) are considered, it is assumed that ϕ_l and ϕ_g take the following form:

$$\phi_l = F(y) e^{(\omega t + ikx)}; \qquad \phi_g = G(y) e^{(\omega t + ikx)} \tag{7}$$

When these representations are used for the velocity potentials, the solution of Laplace's equation subject to the boundary conditions noted can be shown to be

$$\phi_l = \eta_0 (\omega / k) \tanh(kh) e^{(\omega t + ikx)} \tag{8}$$

for the liquid and

$$\phi_g = \frac{\eta_0}{k} \left[\frac{\cosh(ky) - \tanh(nkh)\sinh(ky)}{\sinh(ky) - \tanh(nkh)\cosh(ky)} \right] (\omega + ik\Delta U) e^{(\omega t + ikx)} \tag{9}$$

for the gas. Substitution of Eqs. (8), (9), and (6) into Eq. (5) at $y = h$ leads to the dispersion relation between the complex growth rate ω and the disturbance wave number k,

$$\omega^2(\rho_l \tanh(kh) D_h - \rho_g N_h) - \omega(2ik\Delta U \rho_g N_h) + k^2 \Delta U^2 \rho_g N_h + \sigma k^3 D_h = 0 \tag{10}$$

where

$$N_h = \cosh(kh) - \tanh(nkh)\sinh(kh) \tag{11}$$

$$D_h = \sinh(kh) - \tanh(nkh)\cosh(kh) \tag{12}$$

The dispersion relation can be nondimensionalized using liquid density ρ_l, liquid-phase velocity U_l, and the jet thickness h as dimensions. At the large Weber number ($\rho_l U^2 h \gg \sigma$) limit, we obtain

$$\omega^2[\tanh(k) - \epsilon\Theta] - \omega(2ik\Delta U \epsilon\Theta) + k^2 \epsilon \Delta U^2 \Theta = 0 \tag{13}$$

where we have used

$$\frac{N_h}{D_h} = \frac{1 - \tanh(nk)\tanh(k)}{\tanh(k) - \tanh(nk)} = \Theta \tag{14}$$

Because the condition for instability is where the real part of growth rate is positive, solving this dispersion relation for growth rate and evaluating the effect of changing the three main parameters (h, ϵ, and ΔU) can provide basic data on the growth of a particular instability. One can show that this expression reduces to Squire's result[14] in the limit $n \to \infty$, $\Theta \to -1$. Here, the parameter Θ measures the effect of the finite channel height.

Figure 2 shows the nondimensional growth rate ω_r for antisymmetrical (sinuous) disturbances as a function of k. Here the density ratio ϵ is 0.01, and the channel width to sheet thickness ratio n is 5. Cases of $U_g/U_l = 2$, 4, and 8 are presented. As shown in the result, the liquid sheet instability grows rapidly as the gas velocity grows. Because of the high speed of the gas phase surrounding the liquid sheet, the Kelvin–Helmholtz instability governs the behavior of the liquid sheet. Although the growth rate increases indefinitely as the wave number grows, viscosity and surface tension in actual flows will reduce the growth rate in large wave number region.

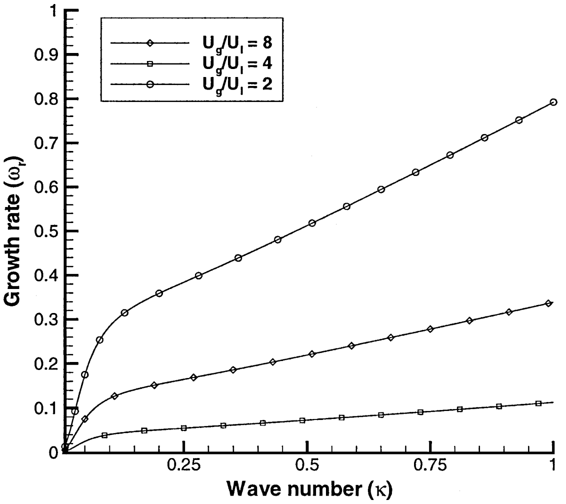

Fig. 2 Effect of gas velocity on growth rate: $\epsilon = 0.01$ and $n = 5$.

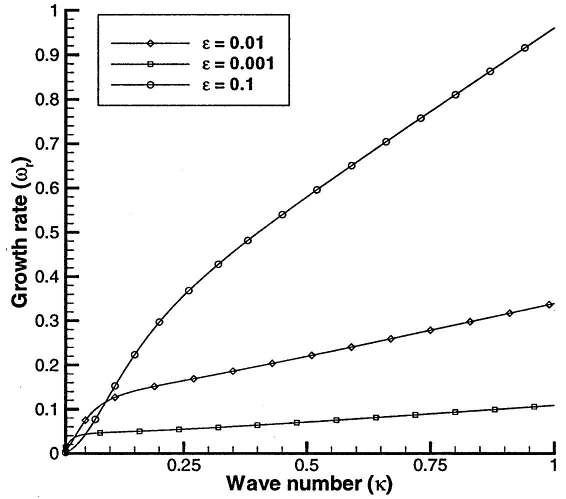

Fig. 3 Effect of gas/liquid density ratio ϵ on growth rate: $\Delta U = 3$ and $n = 5$.

Figure 3 shows the effect of gas/liquid density ratio on growth rate. Here $\Delta U = 3$ and $n = 2$ for all cases, and density ratio ϵ values of 0.1, 0.01 and 0.001 are considered. As the gas-phase density increases, the gas imparts more momentum to the liquid surface. Therefore, the growth rate of disturbance increases when the density ratio gets higher. There are some interesting crossovers in the curves for very long waves corrsponding to low k values.

The effect of channel width to jet thickness ratio n is shown in Fig. 4. The density ratio ϵ is 0.01, the relative velocity ΔU is 3, and n values of 2, 5, and 10 are considered. This result shows that the instability grows rapidly as the sheet gets thicker (channel gets smaller). However, in the small wave number region ($k < 0.07$), the growth rate exhibits the opposite pattern. The presence of the cavity wall has a stabilizing effect on the very long wave instabilities. This behavior is most important in assessing the growth rate response because the long wavelength instabilities are presumed to be the most harmful to overall injector performance in combustion systems. Therefore, one can conclude that the presence of wall can either be a stabilizing or destabilizing effect, depending on the wavelength of the instability.

Modeling Description

A two-dimensional incompressible, unsteady, viscous flow solver has been developed utilizing a finite volume implementation of the marker and cell discretization method. The current model is based on

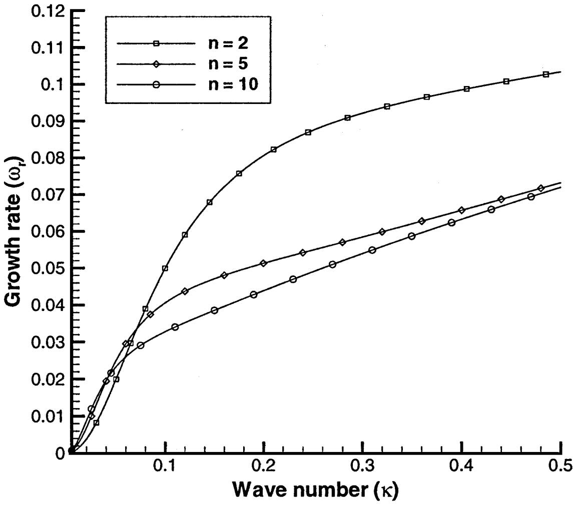

Fig. 4 Effect of channel width on growth rate: $\epsilon = 0.01$ and $\Delta U = 3$.

homogeneous flow two-phase treatment in which the single-phase Navier–Stokes equations are solved using a fictitious pseudo density that varies in amplitude between the liquid and gas extremes. This provides a mechanism to compute the local droplet number density without having to solve the flowfield around all of the individual droplets. The single fluid model can be achieved by assuming locally homogeneous flow (LHF) in which the relative velocity and temperature between two phases are small enough in comparison to variation of the overall flowfield that is to be predicted. Under the LHF assumption, and by providing a proper constitutive relation for the pseudodensity of the homogeneous flow, the model is able to handle the two-phase flow with less computational resources than traditional two-fluid modeling. However, capillary forces are not resolved using this approach because the interface is not known as part of the solution methodology. For the high Reynolds and Weber numbers characterizing the injectors of interest, this simplification is deemed appropriate. The development of the homogeneous fluid model is discussed in detail in Refs. 17–19.

The two-dimensional, viscous, unsteady, Navier–Stokes equations are expressed in the following form:

$$\frac{\partial \rho}{\partial t} + \frac{\partial \rho u}{\partial x} + \frac{\partial \rho v}{\partial y} = 0 \tag{15}$$

$$\frac{\partial \rho u}{\partial t} + \frac{\partial \rho u^2}{\partial x} + \frac{\partial \rho u v}{\partial y} + \frac{\partial P}{\partial x} = \frac{\partial}{\partial x}\mu\frac{\partial u}{\partial x} + \frac{\partial}{\partial y}\mu\frac{\partial u}{\partial y} \tag{16}$$

$$\frac{\partial \rho v}{\partial t} + \frac{\partial \rho u v}{\partial x} + \frac{\partial \rho v^2}{\partial y} + \frac{\partial P}{\partial y} = \frac{\partial}{\partial x}\mu\frac{\partial v}{\partial x} + \frac{\partial}{\partial y}\mu\frac{\partial v}{\partial y} \tag{17}$$

The Lagrangian form of the continuity equation is also required,

$$\frac{\mathrm{D}\rho}{\mathrm{D}t} + \rho\left(\frac{\partial u}{\partial x} + \frac{\partial v}{\partial y}\right) = 0 \tag{18}$$

Because of the two-phase treatment, the viscosity can vary spatially. According to Kubota et al.,[20] the viscosity of mixture can be written as

$$\mu = \alpha\mu_g + (1-\alpha)\mu_l \tag{19}$$

where μ_g and μ_l are the gas and liquid viscosities and α is the void fraction. Because the nondimensional pseudodensity is volume fraction of mass per unit cell volume, Eq. (19) can be written as

$$\mu(\rho) = \rho\mu_l + (1-\rho)\mu_g \tag{20}$$

This mixture viscosity is substituted back into Eqs. (16) and (17) for nondimensionalization. The channel width, liquid inflow velocity, and liquid density are chosen as dimensions in nondimensionalizing the equations. Rearranging the equations for flux calculation through cell faces yields the following momentum equations:

$$\frac{\partial \rho u}{\partial t} + \frac{\partial}{\partial x}\left[\rho u^2 - \frac{1}{Re^*}\frac{\partial u}{\partial x}\right] + \frac{\partial}{\partial y}\left[\rho u v - \frac{1}{Re^*}\frac{\partial u}{\partial y}\right] = -\frac{\partial p}{\partial x} \tag{21}$$

$$\frac{\partial \rho v}{\partial t} + \frac{\partial}{\partial x}\left[\rho u v - \frac{1}{Re^*}\frac{\partial v}{\partial x}\right] + \frac{\partial}{\partial y}\left[\rho v^2 - \frac{1}{Re^*}\frac{\partial v}{\partial y}\right] = -\frac{\partial p}{\partial y} \tag{22}$$

where

$$1/Re^* = (\rho/Re_l) + [\rho_g(1-\rho)/\rho_l](1/Re_g) \tag{23}$$

which includes the both liquid- and gas-phase viscous effect in one term. The second and third terms in left-hand side of Eqs. (21) and (22) are the main terms for calculation of momentum fluxes in x and y directions in the code. Here Re_l and Re_g are Reynolds numbers of liquid and gas phases, respectively.

Because ρ is a nonphysical variable, an additional constitutive relation is required in place of an equation of state that would normally close the set of governing equations. In this case, we envision a group of droplets convecting through a gas media. If we assume all droplets are of the same size and neglect fission or fusion processes, then the local number density sets the pseudodensity for a given computational cell. Consequently, one can conclude from the preceding assumptions that the density evolves in time by simply considering a Lagrangian tracking of the droplet field as specified by a continuity equation as

$$\frac{\mathrm{D}\rho}{\mathrm{D}t} = \frac{\partial \rho}{\partial t} + u\frac{\partial \rho}{\partial x} + v\frac{\partial \rho}{\partial y} = 0 \tag{24}$$

This equation is basically a statement that the droplet mass is invariant along a path line in the fluid. When the flow direction is taken into account, the pseudodensity is updated based on mass flux calculation as follows:

$$\rho^{n+1} = \rho^n - (\Delta t/V_c)\left[(\dot{m}_{\mathrm{out}})_{x,y} - (\dot{m}_{\mathrm{in}})_{x,y}\right] \tag{25}$$

where V_c is volume of a given cell and $\dot{m}$ is mass flow rate in corresponding x and y directions. The flux of the mass through a given cell is calculated by a standard upwind scheme. Whereas this provides a locally first-order solution in the region adjacent to the discontinuity in density, it provides for a stable approach to account for the large-density gradients near the interface. Because the the interface region will undoubtedly contain droplets in these very high convective environments, a shock-type density discontinuity would not be consistent with a homogeneous flow representation. The scheme is second-order accurate with the exception of the points adjacent to the interface, and convergence characteristics are presented in the following section. Figure 5 shows the basic geometry of a coaxial injector. Note that in this case (and the remainder of the work) the sheet thickness is denoted h rather than the half-thickness that was used in the linear analysis. The computational domain is the recessed region inside the nozzle, and the structured mesh employed 100 × 200 grid

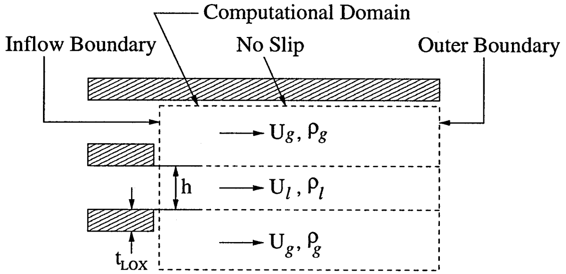

Fig. 5 Coaxial injector schematic noting design variables.

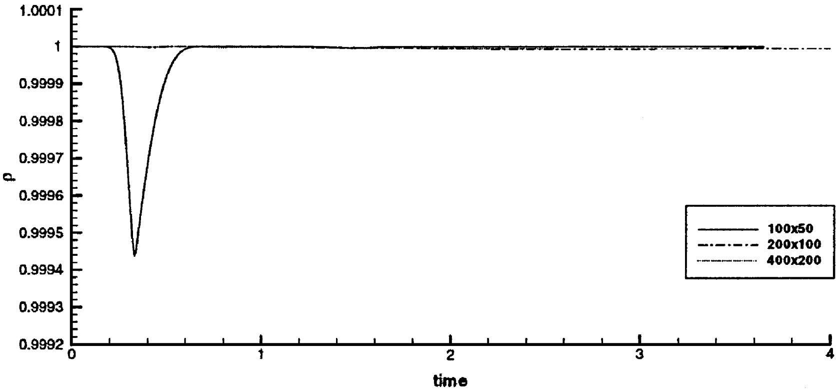

a) Density history

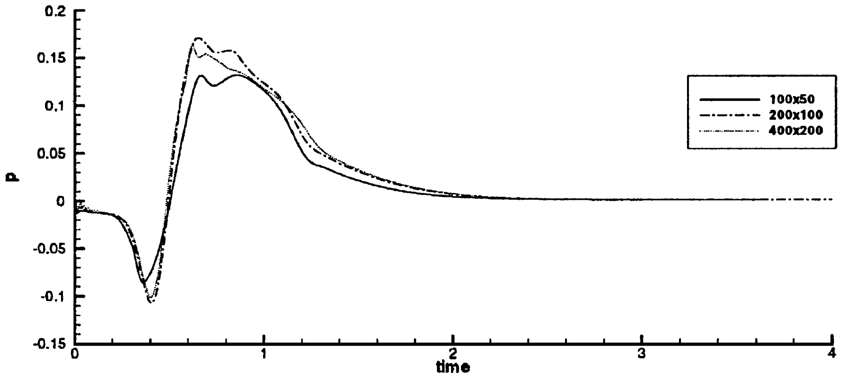

b) Pressure history

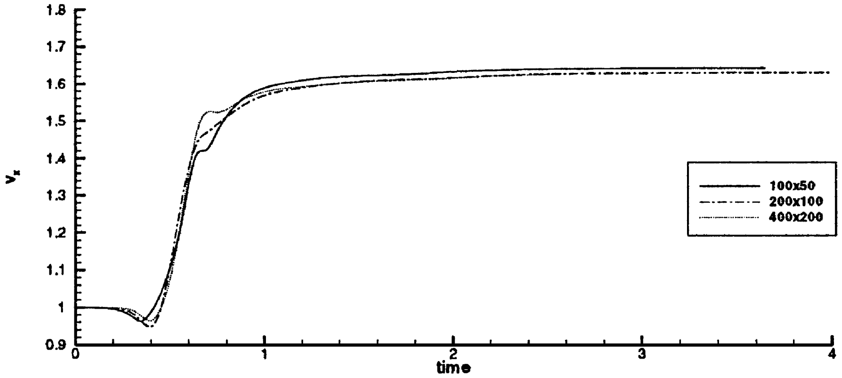

c) Velocity history

Fig. 6 Effect of grid size on density, pressure, and velocity at a point on the centerline of the domain: $U_g/U_l = 4$, $L/D = 2$, $h = 0.2$, and $Re_l = 10^5$.

points in the transverse y and axial x directions, respectively. Exponential stretching is applied in the transverse direction to enhance resolution near the walls.

Liquid- and gas-phase velocities are defined at inflow boundary with pressure computed from a zero-gradient extrapolation from within the domain. No-slip conditions for velocities are defined on both walls. Finally, constant pressure condition is set for outflow boundary, whereas the velocities are extrapolated at this location.

A series of grid convergence studies have verified that this mesh (100 × 200) is adequate to resolve the unsteady sheet flow. Typical flow conditions are utilized for the comparison; after a brief startup discontinuity, the results reach a steady state after a few thousand time steps. The growth rate of the instability is so low for these initial conditions that it takes hundreds of thousands of time steps for the instability to appear. The convergence comparison is made during this early steady-flow stage; fully unsteady convergence has been demonstrated in previous works.[18,19]

A center point in the computational domain has been chosen for a flow-representative position. Time histories of density, pressure, and liquid velocity have been observed until the flow solution reaches steady state. Figure 6 shows the history for each variable at the center point for three grid sizes, 100 × 50, 200 × 100, and 400 × 200, in x and y directions, respectively. The result shows that the 200 × 100 grid provides accuracy comparable to the 400 × 200 grid. In Figs. 7 and 8, the density and velocity transverse profiles at the nozzle exit are compared for the three grids at a time when steady-state conditions are reached. These results clearly indicate the capabilities of the model to resolve density and velocity discontinuities present in these two-fluid flows.

The 200 × 100 mesh was selected for use in the remainder of the studies. A typical calculation takes 3–4 h for the 200 × 100 grid on Pentium II 450–MHz machine. The 400 × 200 grid runs about 48 h even on 64-bit reduced instruction set computer Alpha chip (500–MHz) machine until the flow solution reaches steady state.

Because it takes a substantially long time until the liquid sheet develops the instability from roundoff errors and the development of boundary layers, an artificial disturbance is introduced to initiate the oscillation at an ealier stage. This has been accomplished by introducing unbalanced velocities on upper and lower sides of the liquid surface grid points at the initial time step ($t = 0.0$) only.

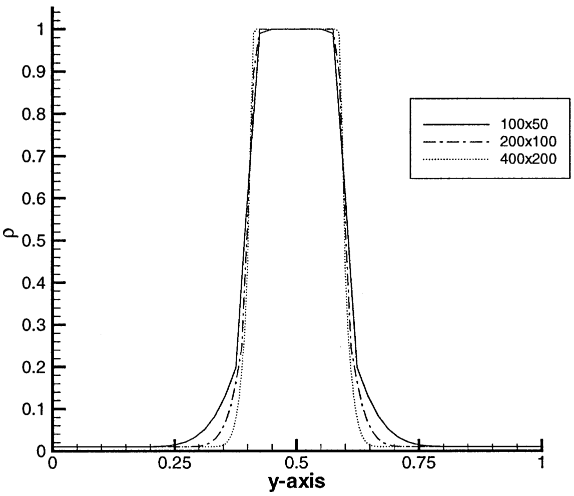

Fig. 7 Density distribution at exit at steady state.

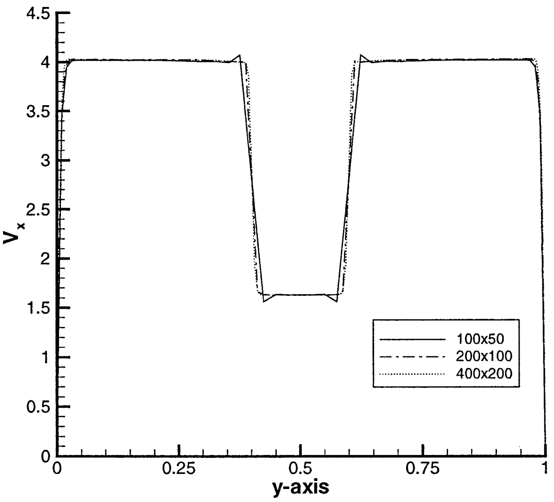

Fig. 8 Velocity distribution at exit at steady state.

The result shows that a certain level of small disturbance can cause the violent oscillation of the liquid sheet inside the channel after a short transient time. Because the flowfield is solved by a system of elliptic–parabolic governing equations, the numerical disturbance causing the oscillation is initial-condition dependent. Simulations without the unbalanced velocities show the same limit-cycle behavior, although these calculations take a very long time. Because both techniques produce equivalent nonlinear oscillation amplitudes and frequencies, the unbalanced velocity approach is used for the results presented in the following section.

Numerical Results

A baseline case is presented to provide insight into the unsteady jet oscillation inside a coaxial injector nozzle. The injector schematic is shown in Fig. 5. The channel width is assumed to be 0.005 m, and the liquid sheet width is 0.001 m. The length of recessed region L is 0.01 m, which is twice the channel diameter. The thickness of liquid injector post structure is neglected in this baseline simulation. The gas and liquid phase velocities are 80 and 20 m/s, respectively. The Reynolds numbers are $Re_g = 2.22 \times 10^5$ for gas and $Re_l = 9.98 \times 10^4$ for liquid. Here, density of water has been used for the liquid phase and a gas/liquid density ratio of 0.01 is assumed to be realistic with high-pressure injector operation.

The overall behavior of the instability is shown in Fig. 9, which shows pseudodensity contours at various times during the calculation. Here, the outermost contour is for $\rho_g = 0.01$, and the innermost contour is for $\rho_l = 1.0$. After some chaotic oscillations during early phases of the calculation, the sheet enters a quasi-periodic oscillation. The velocity streamlines and velocity profiles at the exit are shown in Fig. 10, indicating the flapping motion of the sheet.

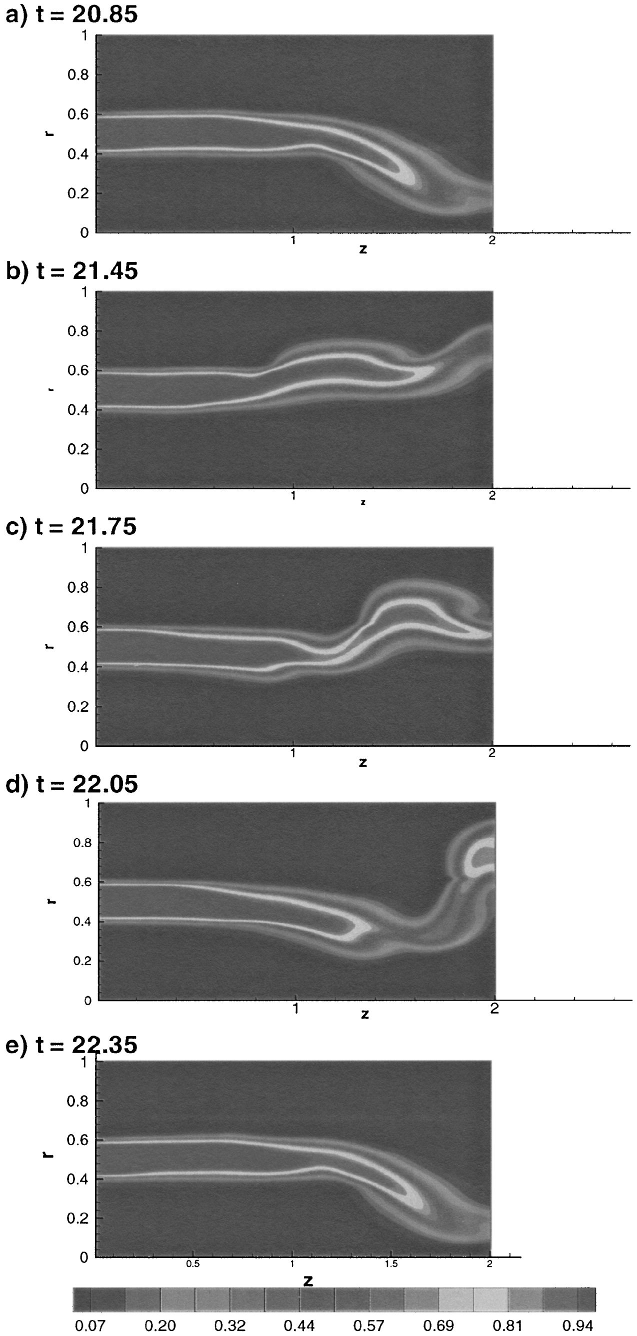

Fig. 9 Density contours in a typical jet oscillation: $U_g/U_l = 4$, $L/D = 2$, $h = 0.2$, and $Re_l = 10^5$.

When the location of maximum density is plotted at the exit plane as a function of time, the character of the oscillation becomes apparent, as seen in Fig. 11, which shows a very high-amplitude oscillation (channel walls at $r = 0, 1$) as evidenced in the pseudodensity contours in Fig. 9.

The oscillation is also quasi periodic; by taking the fast fourier transform (FFT) of the signal in Fig. 11, we can identify its fundamental frequencies. Results of this calculation are shown in Fig. 12. The peak near $f = 0$ is attributed to the steady part of the signal. The first peak with frequency of 0.6836 indicates the fundamental frequency, and the second peak corresponds to the first harmonic mode at frequency of 1.3867. The development of multiple harmonics takes longer than for a single tone. There is some activity at higher harmonics, but at a much lower energy level than the primary tone and the first harmonic. Under the nondimensionalization

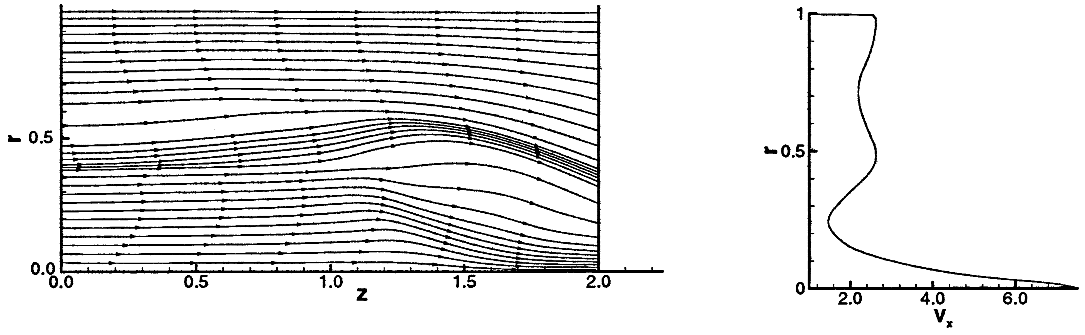

a) $t = 20.85$

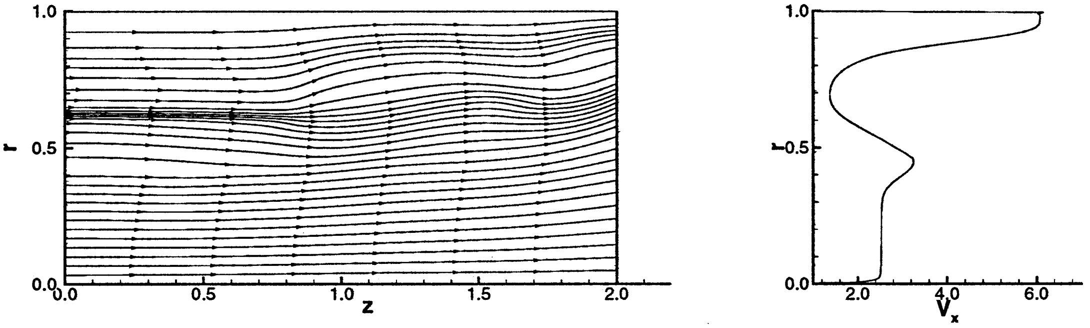

b) $t = 21.45$

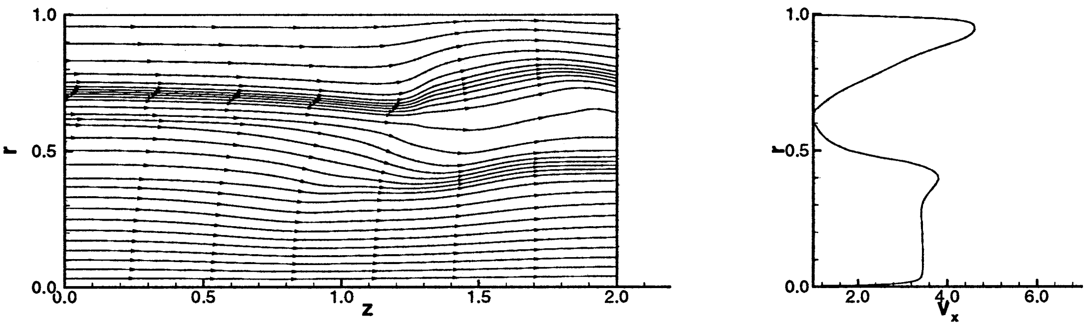

c) $t = 21.75$

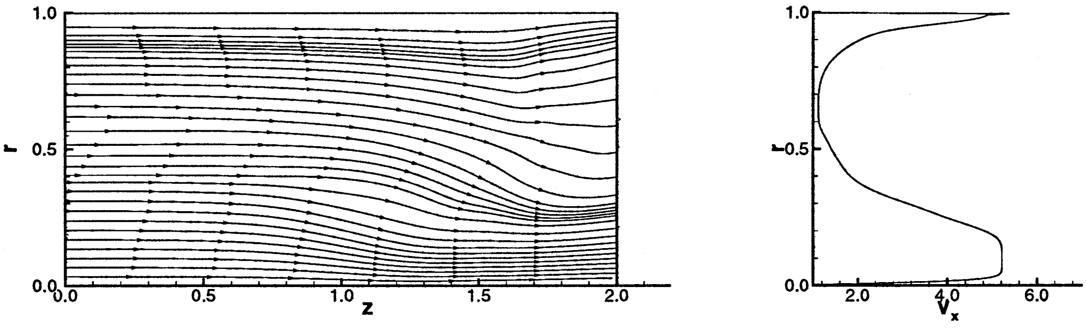

d) $t = 22.05$

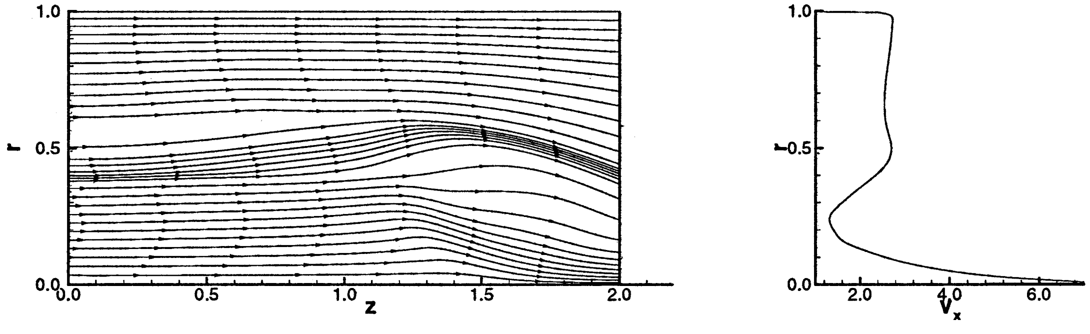

e) $t = 22.35$

Fig. 10 Velocity streamlines and exit velocity profiles in a typical jet oscillation: $U_g/U_l = 4$, $L/D = 2$, $h = 0.2$, and $Re_l = 10^5$.

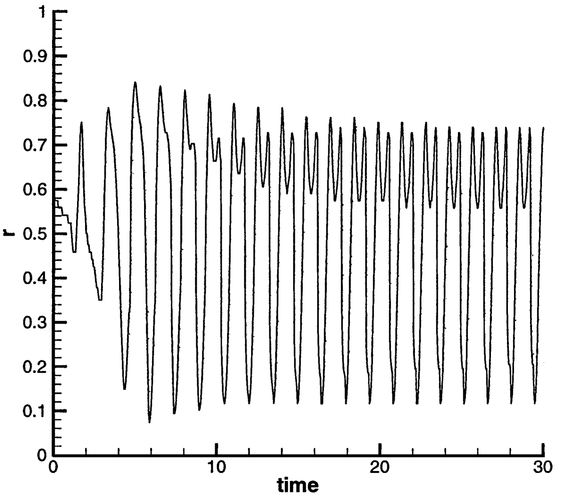

Fig. 11 Liquid sheet oscillation, maximum density location at channel exit: $U_g/U_l = 4$, $L/D = 2$, $h = 0.2$, and $Re_l = 10^5$.

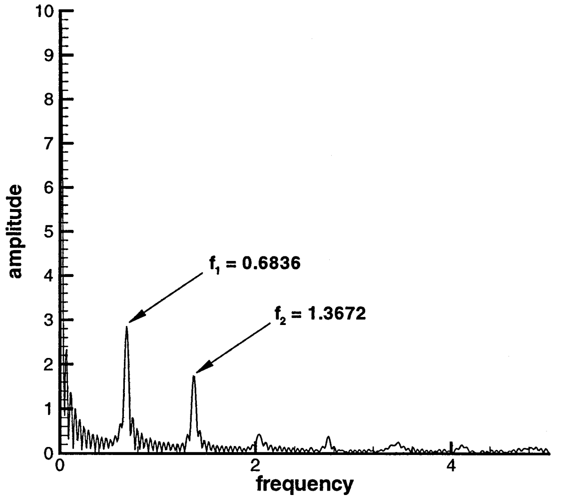

Fig. 12 FFT analysis of liquid sheet oscillation.

employed, a frequency of 2.0 would correspond to the time it takes a liquid fluid element to traverse the channel according to the definition of Strouhal number. The primary tone would correspond to a period of roughly three times the channel transit time.

When these nondimensional frequency values are converted into physical ones, the primary harmonic is at 2740 Hz, and the second harmonic is near 5600 Hz. These are frequencies within the range of acoustic modes within liquid rocket engine combustion chambers. A series of experimental results by Eroglu and Chigier[12] also showed that the frequencies of jet oscillation of air-blast coaxial injector at similar water/air velocities fall into the same frequency band. In principal, the numerical analysis does support the conclusion that jet instability in the submerged region could reinforce instabilities in the combustion chamber. However, the jet submergence is much larger here than that typically used in rocket engine injectors. For this reason, a parametric study was initiated to classify the instability over a range of design and operating conditions.

Parametric Study

A parametric study has been conducted to evaluate the influence of gas/liquid density ratio, velocity ratio, sheet thickness, sheet submergence, and Reynolds number. Results are compared by plotting the amplitude of the oscillation (basically the difference between the upper peaks and lower peaks in Fig. 11) as a function of time for the various parameters investigated.

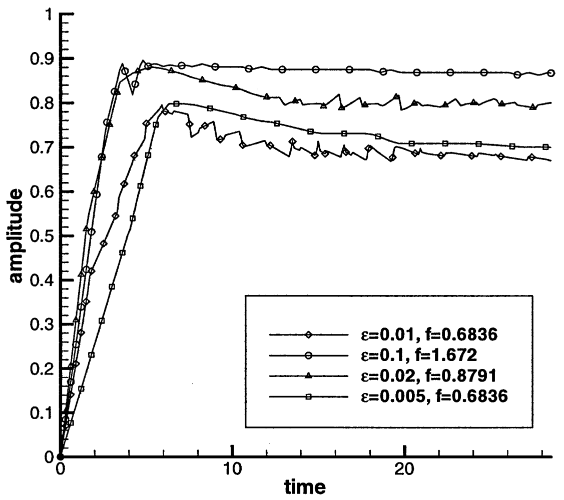

Fig. 13 Effect of density ratio on amplitude of the sheet oscillation: $U_g/U_l = 4$, $L/D = 2$, $h = 0.2$, and $Re_l = 10^5$.

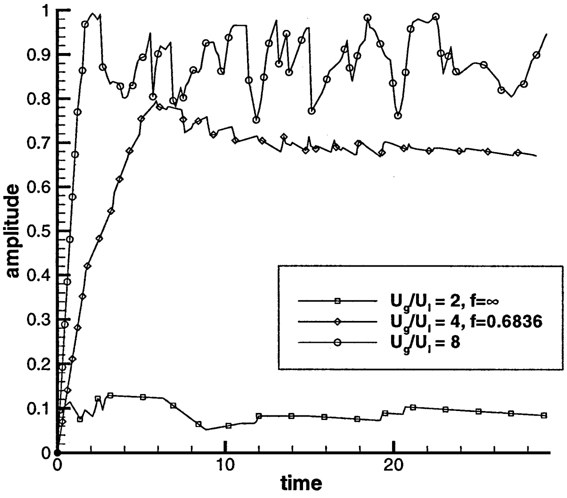

Fig. 14 Effect of velocity ratio on amplitude of the sheet oscillation: $\epsilon = 0.01$, $L/D = 2$, $h = 0.2$, and $Re_l = 10^5$.

Density Ratio Effects

Four simulations at various gas/liquid density ratios with all other inputs fixed ($U_g/U_l = 4$, $L/D = 2$, $h = 0.2$, and $Re = 10^5$) have been conducted to assess the influence of this parameter. The oscillation amplitude histories for these cases are summarized in Fig. 13 for gas/liquid density ratios $\epsilon = 0.005$, 0.01, 0.02, and 0.1. The primary frequency f of each case is also noted in the legend in Fig. 13. Results indicate that both the amplitude and the frequency of the oscillation increase with gas density. Physically, this is because the gas is capable of imparting more momentum to the liquid when it is of higher density. This behavior is completely consistent with the linear Kelvin–Helmholtz theory.

Effect of Gas/Liquid Velocity Ratio

Three different velocity ratio cases have been studied for other conditions consistent with the baseline case described earlier. Here, $U_g/U_l = 2$, 4, and 8 were investigated; results are shown in Fig. 14. The case with $U_g/U_l = 2$ shows very little activity because the sheet deviates little from its initial height. The case with $U_g/U_l = 8$ setting shows a chaotic oscillation, which essentially encompasses the entire width of the channel. In this case, it appears that the sheet breaks up because of the unusually high gas velocity, and the liquid fragments disintegrated from the liquid core keep hitting walls and generate nonperiodic, high-frequency vibration rather than wave-type oscillation. For this reason, no frequency value is reported for this condition.

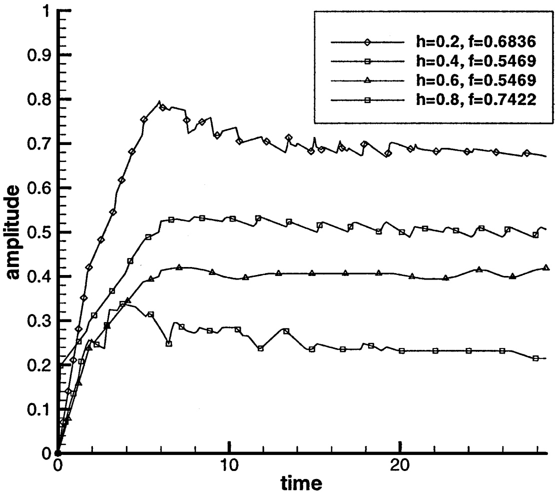

Fig. 15 Effect of jet thickness on amplitude of the sheet oscillation: $U_g/U_l = 4$, $\epsilon = 0.01$, $L/D = 2$, and $Re_l = 10^5$.

Physically, the gasdynamic pressure that drives the instability scales as the square of the gas velocity. The results obtained in this study are consistent with this general nonlinear behavior.

Effect of Varying Sheet Thickness

Geometric variations were also investigated in the studies. Figure 15 shows the influence of the thickness of the liquid sheet at other conditions corresponding to the baseline case. Sheet thicknesses h corresponding to 20, 40, 60, and 80% of the channel width were considered in the study. Physically, this would correspond to thicknesses of 1, 2, 3, and 4 mm in the baseline injector design. In general, the oscillation frequencies were not strongly dependent on the thickness of the sheet. The amplitude of the oscillations tends to decrease with increasing h presumably because the liquid inertia grows with the sheet thickness.

Linear analyses indicate that the presence of the walls has a destabilizing effect, which is the opposite of the trends noted in the nonlinear calculations. The long wave instabilities that govern the calculations are indeed damped by the presence of channel walls. High-frequency, short wave instabilities are not resolved in the present model because capillary forces are neglected and the pseudofluid treatment does not support a sharp discontinuity at the interface. This area would require further study with a separate flow two-phase model to resolve this issue more fully.

Channel Length Effects

The effect of liquid injector submergence is addressed in Fig. 16. Here, the liquid injector was recessed at four separate distances, 1, 1.5, 2, and 3 channel heights ($L/D = 1$, 1.5, 2, 3), with other conditions remaining identical to the baseline configuration. When the channel width is the same as the recess length ($L/D = 1$), there is little activity, and a straight sheet comes out of the exit. As the submergence length is increased, the $L/D = 1.5$ case shows the sheet starts oscillating, but the magnitude of the oscillation is smaller than the baseline case and damps out gradually as time goes on. At $L/D = 2$, large-amplitude oscillations are noted.

At $L/D = 3$, the oscillation becomes chaotic with varying magnitude. In this case, the liquid sheet breaks up before it reaches to the exit, and the liquid fragments from the disintegration near the exit are shot out at somewhat irregular intervals. The radical change of the amplitude of this case can be explained by this behavior. In general, these trends are in agreement with the linear theory because increased submergence increases the time for instabilities to grow within the channel. Because most liquid rocket injectors of this type use very small submergence lengths, the present analysis shows little evidence of instability from the mechanism investigated in this work.

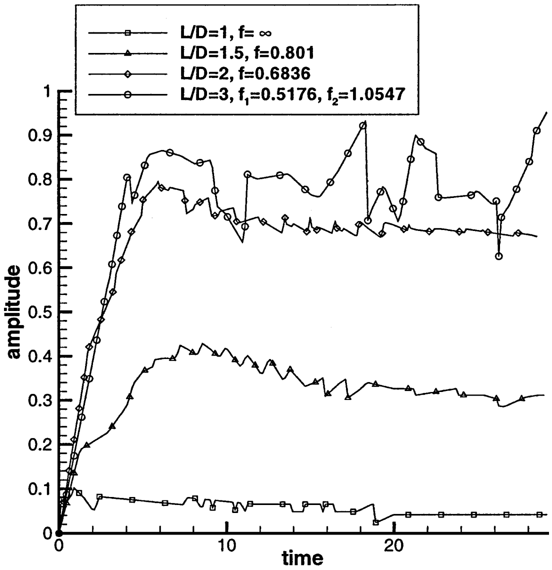

Fig. 16 Effect of channel length on amplitude of the sheet oscillation: $U_g/U_l = 4$, $\epsilon = 0.01$, $h = 0.2$, and $Re_l = 10^5$.

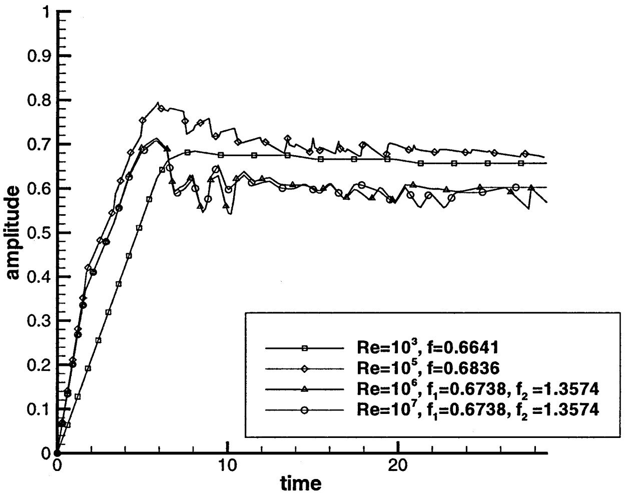

Fig. 17 Effect of gas Reynolds number on amplitude of the sheet oscillation: $U_g/U_l = 4$, $\epsilon = 0.01$, $L/D = 2$, $h = 0.2$.

In general, the frequency of the instability tends to decrease with increased submergence. However, the FFT of the $L/D = 3$ case is interesting in that two distinct frequencies with similar energy content are noted. A short frequency consistent with a long wave instability is present in addition to a higher frequency representative of clumps of disintegrated fluid. For very short submergence lengths, there simply is not time to grow instabilities to any appreciable level under the Kelvin–Helmholtz mechanism.

Reynolds Number Effects

The influence of viscous interactions were investigated through a series of simulations at Reynolds numbers between 10^3 and 10^7. Once again, the other input parameters were maintained at values selected in the baseline configuration. As we can see from the Fig. 17, the amplitude of the oscillation is only slightly affected over this substantial Reynolds number range. In cases of high Reynolds numbers, however, two distinct frequencies appear in the oscillation: a fundamental frequency and a first harmonic mode at a lower energy level. The higher frequency is created by liquid fragments separated from the liquid sheet breakup near the exit. Because the liquid fragments come out of the nozzle exit in a very regular manner, the short wave pattern at high frequency is developed. The amplitude of the oscillation at high Reynolds number decreases slightly because of energy loss caused by the harmonic mode development.

This result is consistent with general nonlinear behavior because decreased viscous interaction generates a higher frequency mode in addition to the primary oscillation.

Effect of Liquid Post Thickness

In this section, the baseline flow conditions are considered with a liquid sheet with a finite post thickness. This structure is often referred to as the LOX post in coaxial injectors involving this cryogenic propellant. When we consider a finite thickness of the post, the flow must now expand/recirculate to fill the region immediately downstream of the post tip. A pair of counter-rotating vortices become apparent immediately downstream of the upper and lower posts. The recirculation region has approximately the same thickness as the post tip thickness t_{LOX} at the nozzle exit and tapers to zero at some downstream point. This recirculation area serves as flame holder in combusting system and stabilizes the liquid jet inside the injector by anchoring the jet to the nozzle exit.

Moon[21] investigated a coaxial injector and showed that the recirculation region exists immediately after the LOX post exit. He explained that the recirculation region is caused by at least two mechanisms: viscous mixing and pressure gradient. Because static pressure is not constant throughout the flow, the recirculation zone forms a pseudodiffuser, causing a low-pressure region to exist near the post tip. Viscous effects cause a slightly more rapid decrease in velocity at the jet boundary.

Glogowski and Micci[11] conducted a series of experiments and investigated the flow near the LOX post region. Unfortunately, measurement of the flow inside the recessed region did not produce favorable results due to difficulties involved in characteristically high signal-to-noise ratio in this area. However, they did verify the recirculation region near the LOX post by measuring mean axial velocity and showing that there exists negative mean velocity at the post tip. For the condition where the LOX post thickness is not negligible, they agreed that macroscopic instability within the liquid jet arise from both static pressure perturbations and aerodynamic viscous forces. In research of Glogowski et al.,[10] the flow characteristics of recessed LOX post area was investigated. They found that the injection operation with tapered LOX post recessed into fuel annulus produced a resonance condition characterized by a whistling noise and a significant modification to the overall spray structure. The nontapered (straight) post exhibited a lower amplitude whistling noise but did not affect the spray structure.

All of the flow properties used in the preceding baseline case are preserved except the liquid post now has a finite thickness with solid wall no-slip boundary conditions. To improve resolution in the liquid post exit area, the spacing in the x direction is exponentially stretched by using the same strategy used in y-direction stretching. The smallest grid size is applied to the area between the gas and liquid phase, where the most interaction is expected. The liquid post thicknesses here are 0.1 each in unit channel width. Dimensional conversion gives each 0.5 mm thickness of the upper and lower post in 5-mm channel width. Note that the no-slip boundary condition is defined on the post tip in the y direction. The other boundary conditions remain the same as the baseline case without liquid post thickness.

Figure 18 shows pseudodensity contours at various times. The liquid sheet develops symmetric disturbances on its surface due to expansion of the flow into the bluff region downstream of the posts (Fig. 18a). The length of this region is about 5 or 6 times the post tip thickness. After this calculation startup period, the liquid sheet enters a fiber-type breakup mode,[7] which creates continuous surface vortices showing aerodynamic viscous effects (Fig. 18b). This limit-cycle, bounded-oscillation state lasts until instability of the liquid sheet itself becomes prominent and starts to generate an asymmetric wave (Fig. 18c). This wave grows rapidly, and the liquid sheet oscillates in a quasi-periodic manner (Figs. 18d and 18e). When compared with the baseline case without liquid post thickness, the oscillation is larger in magnitude and has a shorter wavelength, leading to a higher frequency.

Velocity streamlines and exit velocity profiles are shown in Fig. 19. The flow recirculation at the liquid post exit is obvious in Fig. 19. Symmetric recirculation regions are developed on upper and lower surfaces during the initial and bounded oscillating state periods (Figs. 19a and 19b). The velocity profiles at the injector exit in this period show the momentum deficit in the radial areas corresponding to the upper and lower posts. During this period, one can see the assumed plug-flow velocity distribution in the liquid is largely maintained. Once the liquid sheet starts to oscillate, the velocity profile goes through a corresponding oscillation. Note that the highest density region is actually convected out of the channel with the highest velocity (Figs. 19d and 19e) even though the liquid is injected at lower velocity than the gas. These velocity profile characteristics show the same qualitative behavior as the results of the measurements by Moon[21] and Glogowski et al.[10].

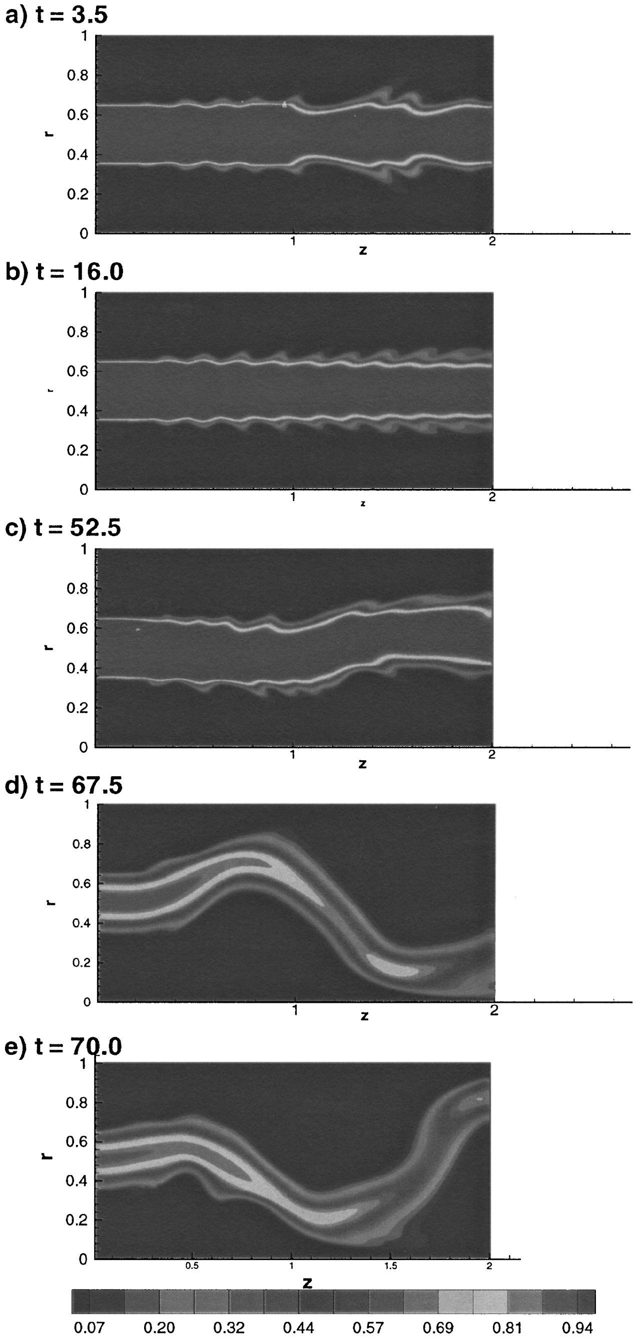

Fig. 18 Density contours liquid sheet oscillation with liquid post thickness: $t_{\mathrm{LOX}} = 0.1$, $U_g/U_l = 4$, $L/D = 2$, $h = 0.2$, and $Re_l = 10^5$.

Two different liquid post thickness have been evaluated to assess the influence of this parameter. Posts of twice ($t_{\mathrm{LOX}} = 0.2$) and half ($t_{\mathrm{LOX}} = 0.05$) of the baseline thickness were considered. The magnitude of oscillation of each LOX post thickness are plotted with the previous baseline case without finite post thickness in Fig. 20. Note that the lines are plotted only for the oscillation period, that is, the initial point $t = 0.0$ is when the quasi-periodic oscillation starts. For the thicker post case, larger surface vortices are formed initially due

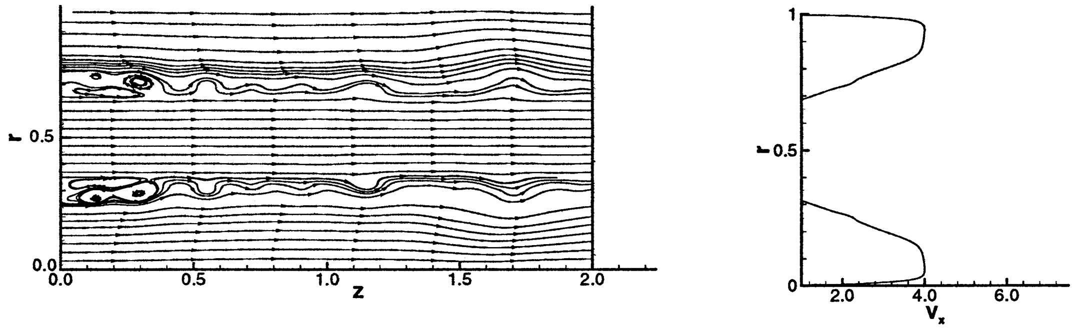

a) $t = 3.5$

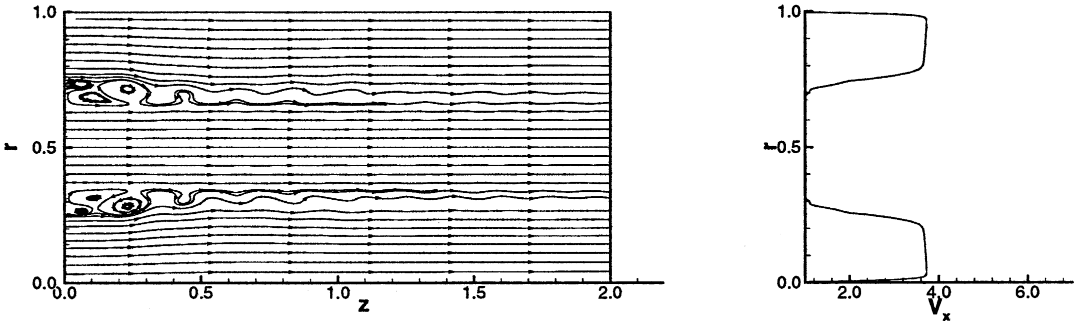

b) $t = 16.0$

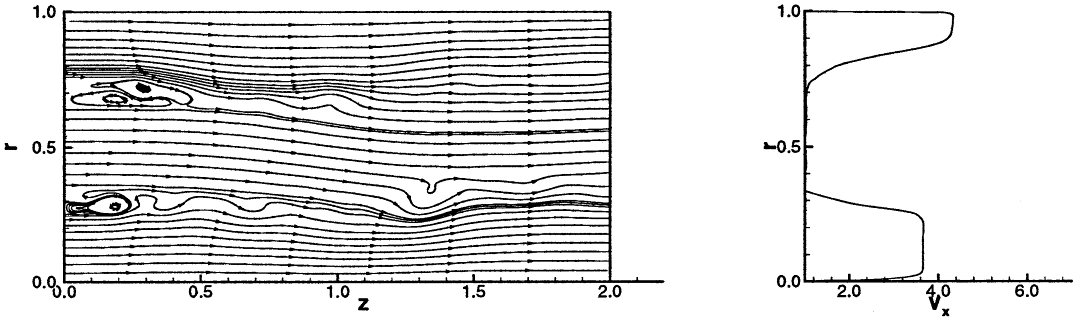

c) $t = 52.5$

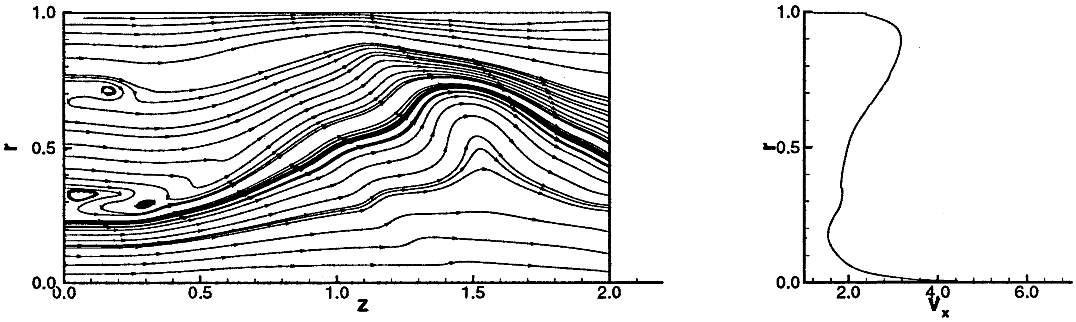

d) $t = 67.5$

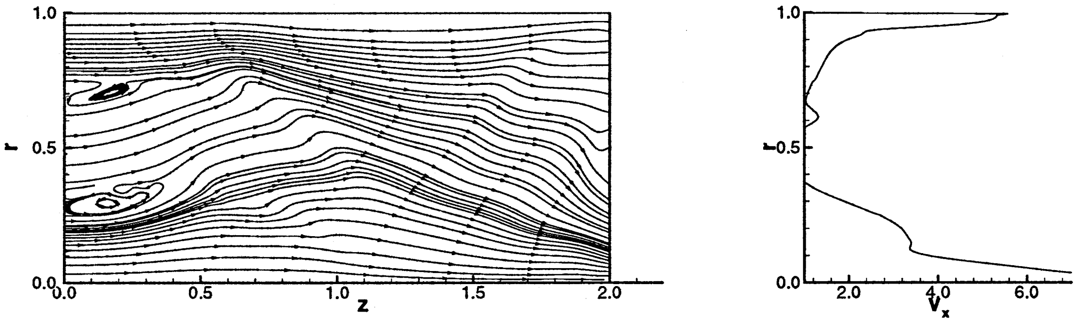

e) $t = 70.5$

Fig. 19 Velocity streamlines and exit velocity profiles with liquid post thickness: $t_{\mathrm{LOX}} = 0.1$, $U_g/U_l = 4$, $L/D = 2$, $h = 0.2$, and $Re_l = 10^5$.

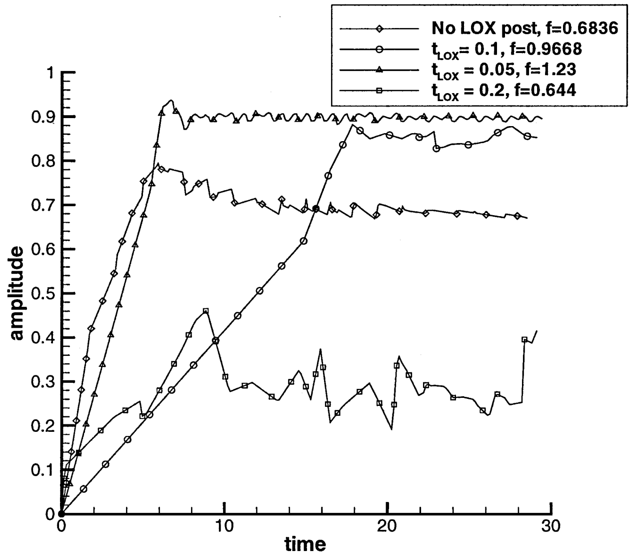

Fig. 20 Effect of liquid post thickness on amplitude of oscillation: $U_g/U_l = 4$ and $L/D = 2$.

to bigger recirculation region at the post tip. The liquid sheet then undergoes a quasi-periodic oscillation with an amplitude much less than that of the $t_{\mathrm{LOX}} = 0.1$ case. The intact length of the liquid sheet from the base of the liquid post is increased in this case, and the frequency of the oscillation is lower than the $t_{\mathrm{LOX}} = 0.1$ case. In the thinner liquid post configuration, the long wave disturbance appears almost immediately, and the magnitude of the oscillation grows to about the same level as the $t_{\mathrm{LOX}} = 0.1$ case, but with a significantly higher frequency of oscillation.

In comparing these results to the case from the preceding section, where the post thickness was neglected altogether, we see interesting behavior. The thicker post shows a stabilizing effect, whereas the two thinner posts show amplification in the instability as compared to the case where a zero post thickness was assumed. These results indicate that that the thickness of the post can play a strong role in the instability and can, in principle, explain the significant differences in spray character noted by Glogowski et al.[10] when tapered and untapered posts were used.

Conclusions

A homogeneous flow model has been developed to assess hydrodynamic instabilities of coaxial atomizers in which a liquid jet/sheet is submerged slightly in an annular gas stream. The calculations have been performed in a two-dimensional analog to this geometry: a liquid sheet with coflowing gas on upper and lower extremities. Kelvin–Helmholtz type instabilities are noted under conditions where the gas velocity is substantially greater than that of the liquid. Parametric studies indicate the amplitude of the instability increases with gas velocity, gas density, and sheet recess/submergence length inside the channel. Increasing sheet thickness tended to decrease the amplitude of the oscillation. The frequencies observed are consistent with the channel transit time of the liquid.

A series of liquid post thicknesses were investigated to assess the effects of this parameter. Flow recirculation at the post tip is observed in accordance with previous experimental observations. Thin posts show greater amplitude instabilities than the zero-thickness case, whereas a thicker post proved to damp the amplitude of the oscillation. In addition, the thinner posts created much higher oscillation frequencies than the case of a zero-thickness post. These results are indicative of the effects noted experimentally; strong differences in exit flow can be attributed to fairly minor changes in post thickness.

Acknowledgment

The authors acknowledge the support of the U.S. Air Force Office of Scientific Research, under Grant F49620-99-1-0092 monitored by Mitat Birkan.

References

[1] Bazarov, V. G., and Yang, V., "Liquid-Propellant Rocket Engine Injectors Dynamics," *Journal of Propulsion and Power*, Vol. 14, No. 5, 1998, pp. 797–806.

[2] Bazarov, V. G., and Lyul'ka, L. A., "Nonlinear Interactions in Liquid Propellant Rocket Engine Injectors," AIAA Paper 98-4039, July 1998.

[3] Arai, T., and Hashimoto, H., "Disintegration of a Thin Liquid Sheet in a Cocurrent Gas Stream," *ICLASS-85*, Vol. 1B, 1985, pp. 1–7.

[4] Mayer, W., and Krulle, G., "Rocket Engine Coaxial Injector Liquid/Gas Interface Flow Phenomena," *Journal of Propulsion and Power*, Vol. 11, No. 3, 1995, pp. 513–518.

[5] Mayer, W., and Tamura, H., "Flow Visualization of Supercritical Propellant Injection in a Firing LOX/GH2 Rocket Engines," AIAA Paper 95-2358, July 1995.

[6] Mayer, W., Schik, A., and Schaffler, M., "Injection and Mixing Processing in High-Pressure Liquid Oxygen/Gaseous Hydrogen Rocket Combustors," *Journal of Propulsion and Power*, Vol. 16, No. 5, 2000, pp. 823–828.

[7] Chigier, N., and Reitz, R. D., "Regimes of Jet Breakup and Breakup Mechanisms (Physical Aspect)," *AIAA Journal*, Vol. 3, No. 12, 1995, pp. 109–135.

[8] Hutt, J. J., and Rocker, M., "High-Frequency Injector-Coupled Combustion," *Liquid Rocket Engine Combustion Instability*, Vol. 169, Progress in Astronautics and Aeronautics, AIAA, Washington, DC, 1995, pp. 345–356.

[9] Bazarov, V. G., Puissant, C., Kaltz, T., Milicic, M., and Micci, M., "Self-Pulsations in Coaxial Injectors with Central Swirl Stage," AIAA Paper 94-2774, June 1994.

[10] Glogowski, M., Bar-Gill, M., et al., "Shear Coaxial Injector Instability Mechanisms," AIAA Paper 95-2552, July 1995.

[11] Glogowski, M., and Micci, M. M., "Shear Coaxial Spray Characterization Near the LOX post Tip Region," *Atomization and Sprays*, Vol. 1, 1991, pp. 349–366.

[12] Eroglu, H., and Chigier, N., "Wave Characteristics of Liquid Jets from Airblast Coaxial Atomizers," *Atomization and Sprays*, Vol. 1, 1991, pp. 349–366.

[13] Mansour, A., and Chigier, N., "Dynamic Behavior of Liquid Sheet," *Physics of Fluids A*, Vol. 3, No. 12, 1991, pp. 2971–2980.

[14] Squire, H. B., "Investigation of the Instability of a Moving Liquid Film," *British Journal of Applied Physics*, Vol. 4, 1953, pp. 167–169.

[15] Dombroski, N., and Johns, W. R., "The Aerodynamic Instability and Disintegration of Viscous Liquid Sheet," *Chemical Engineering Science*, Vol. 18, 1963, pp. 203–214.

[16] Li, X., and Tankin, R. S., "On the Temporal Instability of a Two-dimensional Viscous Liquid Sheet," *Journal of Fluid Mechanics*, Vol. 226, 1991, pp. 425–443.

[17] Chen, Y., and Heister, S. D., "Modeling Hydrodynamic Non-Equilibrium in Bubbly and Cavitating Flows," *Journal of Fluids Engineering*, Vol. 118, No. 1, 1995, pp. 172–178.

[18] Bunnell, R. A., "Unsteady, Viscous, Cavitating Simulation of Injector Internal Flows," Ph. D. Dissertation, School of Aeronautics and Astronautics, Purdue Univ., West Lafayette, IN, Aug. 1999.

[19] Bunnell, R. A., Heister, S. D., Yen, C., and Collicott, S. H., "Cavitating Injector Flows: Validation of Numerical Models and Simulations of Pressure Atomizers," *Atomization and Sprays*, Vol. 9, 1999, pp. 445–465.

[20] Kubota, A., et al., "A New Modeling of Cavitating Flows: A Numerical Study of Unsteady Cavitation on a Hydrofoil Section," *Journal of Fluid Mechanics*, Vol. 240, 1992, pp. 59–96.

[21] Moon, L. F., "Pressure and Velocity in a Developing Coaxial Jet," *AIAA Journal*, Vol. 14, No. 1, 1976, pp. 43–49.